Desalination 533 (2022) 115755

Contents lists available at ScienceDirect

Desalination

journal homepage: www.elsevier.com/locate/desal

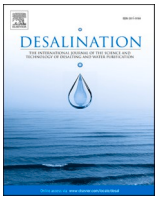

Designing sub-nanometer pores for efficient boron removal

Xin Zhang [a,b], Mingjie Wei [a,*], Yong Wang [a,*]

[a] State Key Laboratory of Materials-Oriented Chemical Engineering, College of Chemical Engineering, Nanjing Tech University, Nanjing 211816, Jiangsu, PR China
[b] College of Safety Science and Engineering, Nanjing Tech University, Nanjing 211816, Jiangsu, PR China

HIGHLIGHTS

- Effects of hydrophilicity, shape, and size of pores on boron rejection are investigated.
- The circular pore is the most suitable to reject boron with high water permeance.
- The hydrophilic pore favors the boron rejection.
- The mechanisms of $B(OH)_3$ rejections are proposed.

GRAPHICAL ABSTRACT

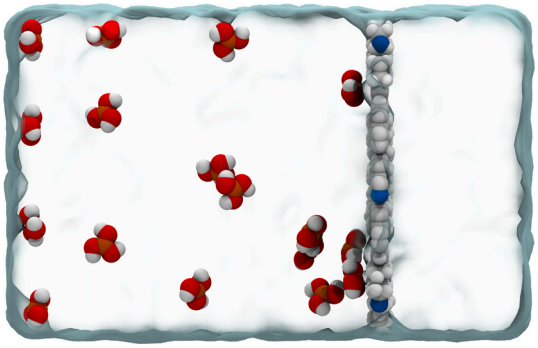

ARTICLE INFO

Keywords:
Boron removal
Reverse osmosis
Nonequilibrium molecular dynamics
Separation mechanism

ABSTRACT

Efficient boron removal is one of the key challenges for reverse osmosis membranes. Understanding the transport behavior of boric acid ($B(OH)_3$) at the molecular level is of great importance to design pores with high permselectivity. Herein, via non-equilibrium molecular dynamics simulations, the $B(OH)_3$ rejection is found to be closely related to the hydrophilicity, shape, and size of sub-nanometer pores. Among these structure parameters, the role of the pore shape is dominant as the slit pore has $\leq$20% $B(OH)_3$ rejections regardless of the pore hydrophilicity and slit width. It is due to the nature of the $B(OH)_3$ molecule being plate-like, even when it is hydrated. Such a unique structure makes the $B(OH)_3$ rejection depend on the major diameter of the non-circular pores. On the other hand, the circular pore, which has the same diameter in all directions, is the most suitable to reject $B(OH)_3$ molecules while providing high water permeance. With a circular pore shape, hydrophilic pores favor the $B(OH)_3$ rejection because the preferentially adsorbed water molecules inside pores can impede the passage of $B(OH)_3$. These findings are expected to guide the rational design and screening of the nanoporous materials for efficient boron removal.

1. Introduction

Water scarcity is one of the major problems in the world due to the rapid population growth and industrialization. As saline water accounts for 97.5% of the global water resource, desalination is recognized as a solution to augment freshwater supply [1]. Owing to the low energy

* Corresponding authors.
E-mail addresses: mj.wei@njtech.edu.cn (M. Wei), yongwang@njtech.edu.cn (Y. Wang).

https://doi.org/10.1016/j.desal.2022.115755
Received 19 February 2022; Received in revised form 23 March 2022; Accepted 29 March 2022
Available online 8 April 2022

consumption, easy operation, and small footprints, reverse osmosis (RO) has become the predominant desalination technology, which accounts for ~70% of the world's desalination capacity [2]. The commercial RO membranes can effectively remove salt ions with a rejection rate of >99% [3]. However, boron is identified as a toxin when the desalted water is firstly found to be poisonous to some crops in the Middle East [4]. The boron ubiquitously exists in seawater with an average concentration of about 4.5 mg/L [5]. Some countries such as China strictly limit the boron concentration of 0.5 mg/L, which requires RO membranes having >90% boron rejection. However, the boron rejections of the commercial RO membranes are commonly <80% [6].

In seawater pH of about 8.4, boron is predominantly present as boric acid, $B(OH)_3$ [5]. Unlike the salt ions, $B(OH)_3$ is a neutral solute with poorly hydration shells, which results in its hydrodynamic size being smaller than that of the hydrated ion. This is why the commercial RO membranes have very high rejections to ions but poor rejections to $B(OH)_3$.

Inadequate $B(OH)_3$ rejection by the single-stage RO process often necessitates additional treatment techniques such as further RO process [7], pH adjustment [8], adsorption [9], or ion exchange [10]. However, these additional treatment processes will increase energy costs and/or the process complexity. If the membranes of single-stage RO achieve the goal of the 90% boron rejection, the additional treatments will be avoided.

To improve the $B(OH)_3$ rejection of RO membranes, some progress has been made to modify the active polyamide layer by incorporating the molecular plugs. However, there is a contradiction in embedding the hydrophobic or hydrophilic molecular plugs. Freger group reported that embedding the hydrophobic glycidyl methacrylate [11] and aliphatic amine molecules [12,13] could facilitate the boron rejection. Wang et al. incorporated the hydrophobic polyisobutylene during the process of the interfacial polymerization, and the boron rejection was increased from 81.36% to 93.12% [14]. Moreover, the incorporation of hydrophilic molecular plugs can also promote the boron rejection. Dydo et al. [15] reported that incorporating the hydrophilic polyol compounds could effectively improve the boron rejection. Zhou group [16] embedded hydrophilic sulfonyl molecules into the polyamide layer to improve the boron rejection from 82.12% to 93.10%. Liu et al. [17] reported that incorporating the hydrophilic UiO-66 nanoparticles can improve the boron rejection to 91.2%.

Based on the findings aforementioned, the understanding of the effect of pore hydrophilicity on the $B(OH)_3$ rejection is controversial. On the one hand, it is considered that the hydrophobic pores are helpful to disrupt the water-$B(OH)_3$ association and decouple the water and $B(OH)_3$ permeation [11,13]. On the other hand, the hydrophilic pore has a strong affinity to the $B(OH)_3$ molecules, which will decrease the diffusion rate of $B(OH)_3$ [16,17]. According to the solution-diffusion mechanism, the hydrophobic pore is not favorable for the process of the $B(OH)_3$ solution, while the hydrophilic pore slows down the process of the $B(OH)_3$ diffusion. Therefore, both hydrophobic and hydrophilic pores seem to favor the $B(OH)_3$ rejection, which confuses the design of membranes for efficient boron removal. Moreover, it is still very challenging to observe the transport behaviors of $B(OH)_3$ in the sub-nanometer pores by any experimental characterizations.

Molecular dynamics (MD) simulations are feasible and powerful techniques to study transport behaviors of fluids in the sub-nanometer pores, which can provide the molecular mechanisms for macroscopic observations. Via MD simulations, a number of studies investigated the effects of size, hydrophilicity, and shape of pores on salt rejection [18–20] and water-ethanol separation [21]. However, the rejection mechanisms of $B(OH)_3$ are rarely investigated. Our previous study reveals a rejection mechanism of $B(OH)_3$. That is, a hydrophilic nanopore preferentially adsorbs water due to the hydrogen bonding interaction, and the pore occupation of water molecules will reject $B(OH)_3$ molecules [22]. However, the effect of the degree of pore hydrophilicity on the $B(OH)_3$ rejection is unrevealed. Besides the pore hydrophilicity, a comprehensive understanding of the effects of the structure parameters of sub-nanometer pores on $B(OH)_3$ rejections is urgently needed.

In this work, the effects of hydrophilicity, shape, and size of pores on the $B(OH)_3$ rejections are systematically investigated via non-equilibrium molecular dynamics (NEMD) simulations. Firstly, to investigate the effect of the pore hydrophilicity on the $B(OH)_3$ rejection, six kinds of functionalized covalent organic frameworks (COFs) with various functional groups (COOH, NH_2, OH, NO_2, SH, and CH_3) but comparable pore diameters are used as pore models. Then, compared with the circular COF pores, the graphene slits are used to investigate the effect of pore shape on the $B(OH)_3$ rejection. After confirming that the circular pore shape is the most suitable to reject $B(OH)_3$ molecules, the role of the diameter of the functionalized COFs is investigated by tuning the chain length of the side groups in the pores.

2. Models and methods

2.1. Models

The size and hydrophilicity of pores were computationally designed based on the experimentally synthesized COF, namely TpPa-1. As shown in Fig. 1a, TpPa-1 is synthesized via the co-condensation of 1,3,5-triformylphloroglucinol (Tp) and *p*-phenylenediamine (Pa) [23]. The unit cell was obtained from the database of CoRE COF [24]. According to the revealed rejection mechanism in our previous studies, the preferentially adsorbed water molecules inside a hydrophilic pore can impede the passage of $B(OH)_3$ [22]. That is, the pore radius can be designed up to the size of a water molecule (~3 Å). Moreover, different functional groups were selected to construct the pores with various degrees of hydrophilicity. Therefore, six functionalized TpPa-Rs, namely -OCC-COOH, -OCCCNH$_2$, -OCCCOH, -OCCCNO$_2$, -OCCCSH, and -OCCCCH$_3$, were built with comparable pore diameters of 6.6, 5.9, 6.6, 5.5, 5.0, and 5.6 Å, respectively (Fig. 1b). The pore size was computationally tuned by changing the length of the side chain and measured by the Zeo++ package [25]. Moreover, our previous studies established the relationship between water contact angles and functional groups in sub-nanometer pores [26]. Since the water contact angle of 65° is regarded as the boundary between hydrophilicity and hydrophobicity [27,28], these functionalized TpPa-Rs can be categorized as hydrophilic (COOH, NH_2, OH) and hydrophobic (NO_2, SH, CH_3) pores.

Firstly, the unit cell of each TpPa-R was optimized by using Cambridge Sequential Total Energy Package (CASTEP). The generalized gradient approximation (GGA) formulated by Perdew-Burke-Ernzerhof (PBE) was used to calculate the electronic exchange and correlation. Then, a TpPa-R membrane composed of four pores was used as models for the following NEMD process.

The snapshot of $B(OH)_3$ and water transport through a TpPa-R membrane is shown in Fig. 2. The $B(OH)_3$ solution in the feed side contains 20 $B(OH)_3$ molecules and 3000 water molecules, corresponding to the boron concentration of 4.0 g/L. A higher boron concentration than seawater (~4.5 mg/L) was used to collect sufficient transport events of $B(OH)_3$ and obtain more precise results in the nanosecond timescale of simulation, which is commonly used in simulation works [29–31]. The number of water molecules in the permeate side was 607. Besides, the transmembrane ΔP in the *z-axis* is generated by applying forces on the two graphene pistons at each side of the system.

2.2. Methods

All the molecular dynamics simulations were performed using the Large-scale Atomic/Molecular Massively Parallel Simulator (LAMMPS) package [32]. The interactions of atoms are composed of the Lennard-Jones (LJ) and Coulombic interactions. The $B(OH)_3$ parameters were proposed by Risplendi et al. [29]. To match the $B(OH)_3$ model, the water model of TIP4P-Ew [33] was used. The bonds and angles of water were constrained by the SHAKE algorithm. The LJ parameters from the

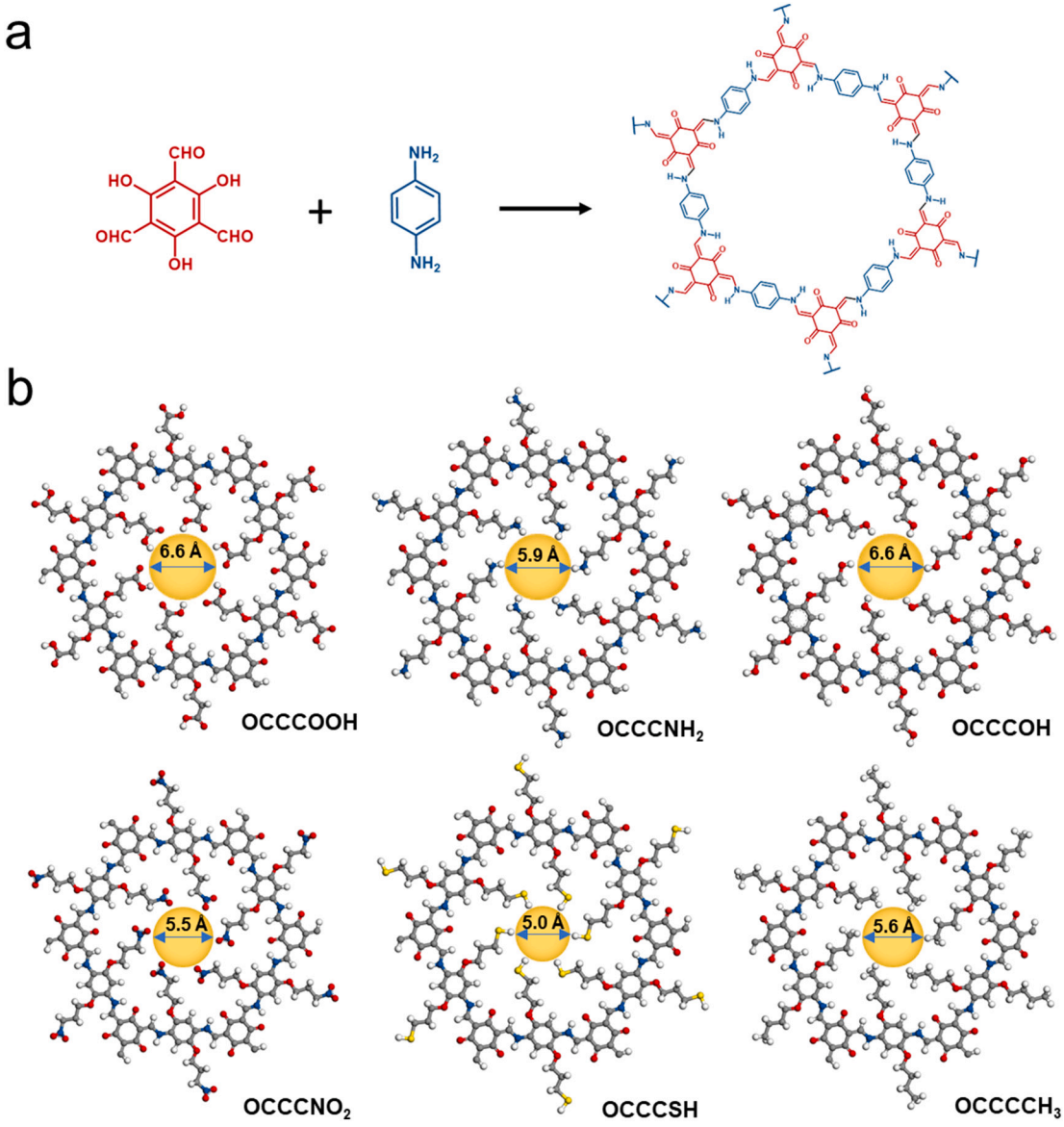

Fig. 1. (a) Schematic of the synthesis of TpPa-1. (b) The atomic structures of TpPa-Rs with terminal groups of COOH, NH_2, OH, NO_2, SH, and CH_3. The yellow circular area represents the location of the pore. The pore diameters are labeled. Atomic colors: C, gray; H, white; O, red; N, blue; S, yellow.

Dreiding force field were used for TpPa-Rs [34], which were widely used in COF-based membranes [35–37]. Restrained electrostatic potential (RESP) charges were used to describe the atomic partial charges of TpPa-Rs, which were given in Table S1. The RESP charges were calculated under the implicit solvent environment of water using B3LYP exchange-correlation functional in conjunction with 6-311G** basis set and analyzed by the Multiwfun [38]. The LJ and Coulombic parameters of graphene slits were described by the optimized potentials for liquid simulations-all atoms (OPLS-AA) [39]. The Lorentz-Berthelot mixing rule was used to calculate pair-wise LJ parameters. Particle-particle particle-mesh (PPPM) solver with a root-mean-square error of 10^{-4} was used to calculate long-range electrostatic interactions [40]. Only x and y directions were set to periodic boundary conditions.

Firstly, energy minimization was performed for each simulation. Then, to let water molecules wet the pores, a 1 ns equilibrium MD simulation was carried out at 0.1 MPa and 300 K. In the NEMD process, a constant pressure (P) is generated by applying an external force (f) on the piston, which can be calculated as:

$$P = \frac{nf}{A} \tag{1}$$

where A represents the membrane area and n represents the atom number of the piston. The two rigid pistons will self-adjust their positions under the pressures to generate the ΔP across the membrane:

$$\Delta P = P_{feed} - P_{permeate} \tag{2}$$

P_{feed} was set to 50.1 MPa and P_{permeate} was set to 0.1 MPa (ambient pressure). The ΔP of 50 MPa was higher than the experimental value, which is commonly used to increase the signal/noise ratio in the limited simulation time [30,31,36]. The system temperature was set to 300 K using the Nosé-Hoover thermostat. The simulation time of the NEMD process is 10 to 120 ns, which allows half of the feedwater to permeate through the membranes. The time step was set to 1 fs. The results were averaged by three parallel runs with different sets of initial configurations.

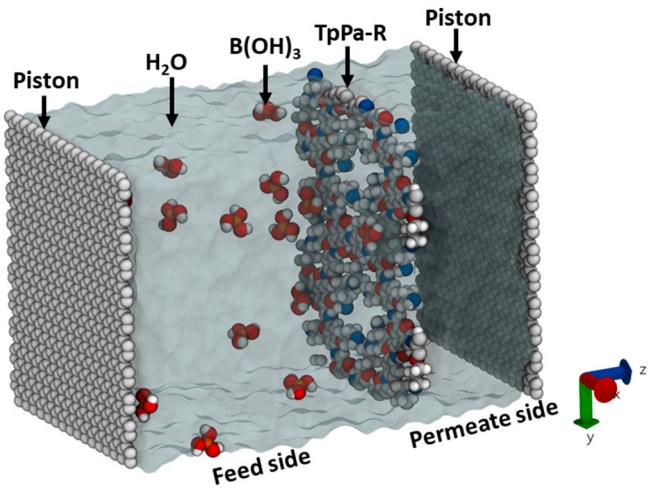

Fig. 2. The snapshot of $B(OH)_3$ and water transport through a TpPa-R membrane. The compositions of the simulation system are labeled.

2.3. Permeance and rejection calculations

As shown in Fig. S2, with the increased sampling time, the number of filtered water molecules is increased linearly, which indicates the steady-state water flows. Water permeance (Q) can be calculated as:

$$Q = \frac{V}{At\Delta P} \tag{3}$$

where V is the volume of permeated water and t is the permeating time. The rejection (R) can be calculated as:

$$R = 1 - \frac{c_p}{c_f} \tag{4}$$

where c_p and c_f represent the concentrations of $B(OH)_3$ in the feed and the filtrate solutions, respectively.

3. Results and discussion

3.1. The effect of functional group on rejection

According to our previous work, the hydrophilicity of the sub-nanometer pores plays a significant role in the $B(OH)_3$ rejection [22]. Therefore, we firstly investigate the $B(OH)_3$ rejections of TpPa-R membranes with various functional groups but comparable pore diameters of ~6.0 Å. As shown in Fig. 3, the $B(OH)_3$ rejections of the hydrophilic pores with functional groups of COOH, NH_2, and OH are 93.4%, 100%, and 100%, respectively. However, the hydrophobic pores with functional groups of NO_2, SH, and CH_3 have $B(OH)_3$ rejections of 12.8%, 19.8%, and 0.1%, respectively. All the hydrophilic pores can meet the standard of the 90% $B(OH)_3$ rejection. However, the $B(OH)_3$ rejection shows a sharp decrease when the pore chemistry changes from hydrophilicity to hydrophobicity. Moreover, taking OH- and H-functionalized TpPa-Rs as examples, the $B(OH)_3$ rejections of the five-layered TpPa-R nanosheet are consistent with those in the monolayer (Fig. S3).

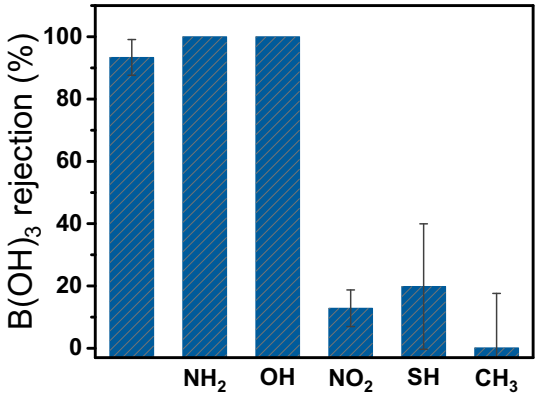

Fig. 3. The rejections of $B(OH)_3$ of the TpPa-R membranes with various functional groups.

Furthermore, we turn to investigate the separation mechanisms. Our previous work indicates that the $B(OH)_3$ has a very weak hydration shell [22]. Therefore, the effect of dehydration cannot explain the huge difference in rejections between hydrophilic and hydrophobic pores. Moreover, it is reported that the $B(OH)_3$ molecule has the Stokes diameter of 3.1 Å [11,41], which is smaller than the diameter of the hydrophilic pores, 5.9–6.6 Å. Therefore, the size exclusion cannot be used to explain the $B(OH)_3$ rejection mechanisms.

Such a huge difference in rejections between the hydrophilic and hydrophobic pores is likely to be caused by the different pore affinities to $B(OH)_3$ and water molecules. Moreover, the breaking and formation of hydrogen bonds (HBs) is reported to play a key role in water transport through nanopores [37]. Therefore, the profiles of the average HB number (n_{HB}) per water molecule along the z-axis in TpPa-R membranes with different functional groups are plotted in Fig. 4. A HB is judged to exist by the geometrical criterion [42]. n_{HB} is ~3.5 in the bulk solution for all cases. In the case of the TpPa-R membrane with the functional group of COOH, n_{HB} between water molecules decreases from 3.5 to 1.6 while water enters the pore. Meanwhile, this HB loss will be compensated by the atoms of the pore wall (PW). n_{HB} from the compensation of the oxygen atoms of the PW (O_{PW}) increases from 0 to 1.1. n_{HB} from the compensation of the hydrogen atoms of the PW (H_{PW}) shows a slight increase near the pore. Considering the HB compensation from the PW atoms, the decrease of total n_{HB} is on a relatively small scale. n_{HB}'s of the HB compensations from COOH, NH_2, and OH are 1.1, 1.0, and 1.0, while those from NO_2, SH, and CH_3 are 0.7, 0.4, and 0.0, respectively. Moreover, the HB lifetimes between water molecules and the functional groups are calculated by HB autocorrelation functions (Fig. S4). The HB lifetimes of water with COOH, NH_2, and OH are 2.1, 16.2, and 5.1 ps, while those of water with NO_2 and SH are 1.5 and 1.2 ps, respectively. The HB lifetime between water and CH_3 was not calculated because there are nearly no HB numbers between them (Fig. 4). By considering the HB numbers and lifetimes, the HB interactions of water molecules with the PW atoms are stronger in the hydrophilic pores. Due to this HB effect, water molecules preferentially adsorb inside the pores, and the occupation of water molecules inside the pore will impede the path of $B(OH)_3$ transport.

To further verify the HB compensation from the PW, the xy-plane density maps for water in the TpPa-R pores are shown in Fig. 5. Inside the hydrophilic pores with the functional groups of COOH, NH_2, and OH, there exist high water densities near the functional groups, which results from the HB interaction between water and the functional groups. These occupied water molecules inside the pore make no room for other molecules to stay, thus making high rejections to $B(OH)_3$. However, inside the hydrophobic pores with the functional groups of NO_2, SH, and CH_3, water densities are relatively uniform near the PW. These water molecules can be replaced by the $B(OH)_3$ molecules because of the weak HB interactions of water molecules with the PW atoms. Moreover, in each TpPa-R membrane, there are also six small pores surrounding the center pores. These small pores do not affect the rejections because they are too small compared to the center pores.

3.2. The effect of pore shape on rejection

As discussed above, the hydrophilic pores with diameters of 5.9–6.6 Å have >90% rejections of $B(OH)_3$. However, the hydrophilic COF-TpTG monolayer with a diameter of 3.9 Å, in our previous work, emerges as low as 64.2% $B(OH)_3$ rejection [22]. It might result from the definition

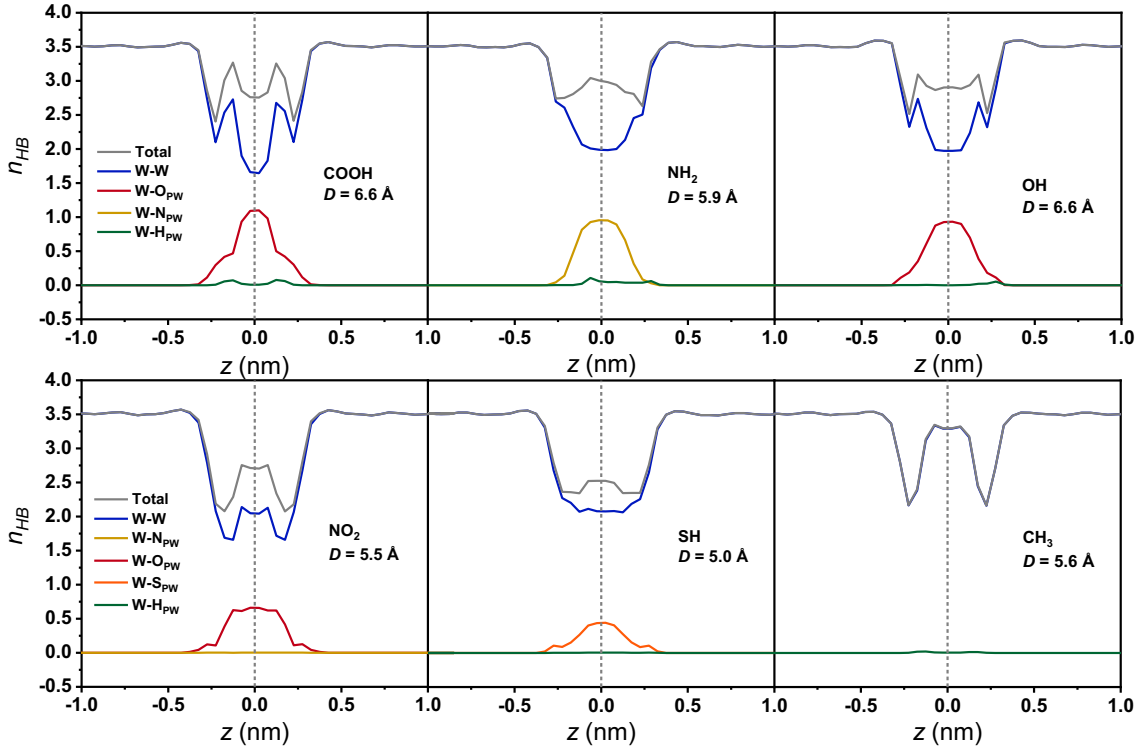

Fig. 4. The profiles of the average HB number (n_{HB}) per water molecule along the *z*-axis in TpPa-R membranes with different functional groups. W-W denotes the HBs between water molecules. O_{PW}, H_{PW}, N_{PW}, and S_{PW} denote the HBs of water molecules with the oxygen, hydrogen, nitrogen, and sulfur atoms of the pore wall (PW), respectively. Total denotes both the two kinds of HBs. The gray dashed line represents the location of the membrane.

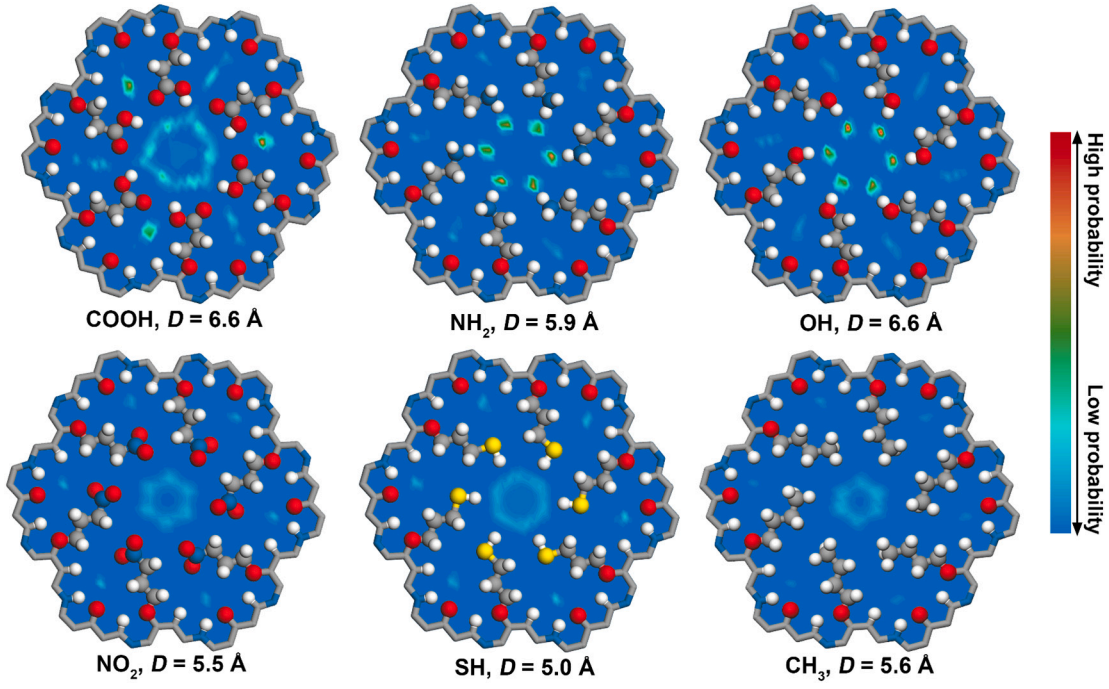

Fig. 5. The *xy*-plane density maps of water in TpPa-R pores with different functional groups.

of pore diameter measured by Zeo++ software. The TpPa-Rs pores are circular but the TpTG pore is triangular (Fig. S5). The diameter is defined by the inscribed sphere in TpTG pores. This reminds us that the shape of the pore should be taken into consideration when investigating the rejection mechanism of $B(OH)_3$.

To further investigate the effect of the pore shape, an extreme case of silt pore is selected in comparison with the above-used circular pores. As shown in Fig. 6a, using typical graphene slits as pore models, the hydrophilic and hydrophobic slits are built by grafting the hydroxyl and hydrogen inside the slits. The $B(OH)_3$ rejections of the slit pores are investigated as shown in Fig. 6b. When the pore diameter is 3.7 Å, the hydrophilic and hydrophobic slits have the $B(OH)_3$ rejections of 20.0%

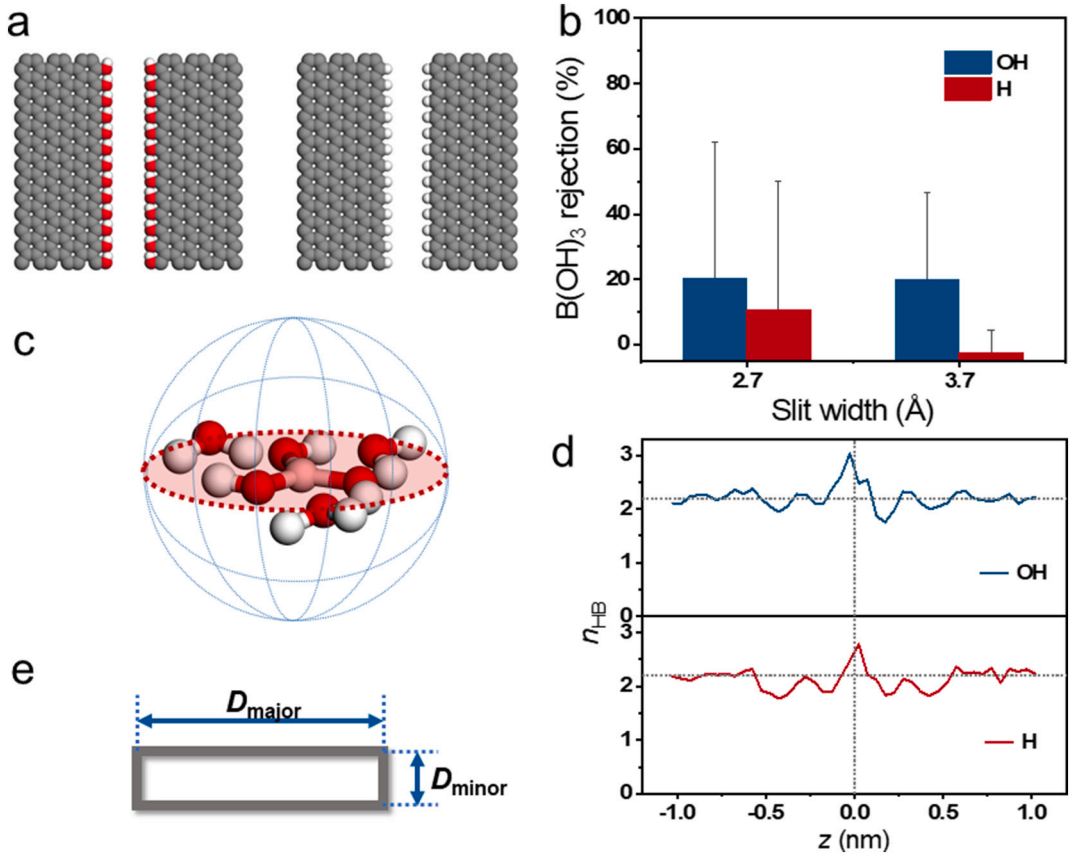

Fig. 6. (a) The atomic structures of hydroxylated (left) and hydrogenated (right) graphene slits. (b) The $B(OH)_3$ rejections of hydroxylated and hydrogenated graphene slits with different slit widths. (c) Schematic illustration of the $B(OH)_3$ molecule with its HB structure with the surrounding water molecules. (d) The profiles of the average HB number (n_{HB}) per $B(OH)_3$ molecule between $B(OH)_3$ and water molecules along the *z-axis* in the hydroxylated and hydrogenated graphene slits with the width of 2.7 Å. The vertical gray dashed line represents the position of the membrane, and the horizontal gray dashed line is $y = 2.2$ (n_{HB} per $B(OH)_3$ molecule in the bulk solution). (e) The schematic illustration for the major and minor diameters (D_{major} and D_{minor}) of a slit pore.

and −2.5%, respectively. When the pore diameter is decreased to 2.7 Å, the hydrophilic and hydrophobic slits have $B(OH)_3$ rejections of 20.2% and 10.6%, respectively. If the pore diameter continues to decrease, the water flux becomes nearly zero. Since water molecules can hardly pass through the membrane, the investigation of the $B(OH)_3$ rejection performance makes no sense. Therefore, it is considered that the slit pore cannot effectively reject $B(OH)_3$ molecules regardless of the pore hydrophilicity and the slit width.

It is recognized that the dehydration of ion passage through a narrow pore leads to the energy barrier, which hinders the ion passage. Similarly, a water molecule can also be regarded to have a hydration shell because of the HB interaction. To enter an extremely confined pore, water molecules will rearrange their hydrogen bonds. This so-called HB rearrangement is often accompanied by the loss of some HB number, which results in the energy barrier for water passage [43,44]. Similarly, the $B(OH)_3$ rejection should be dependent on not only its molecular shape but also its HB interactions with water molecules, i.e., its hydration state.

In the bulk aqueous solution, there exist HBs between the three hydroxyls of one $B(OH)_3$ molecule and the surrounding water molecules. It was calculated that n_{HB} per $B(OH)_3$ molecule in the planar direction of the $B(OH)_3$ molecule is 2.2, while that in the axial direction of the $B(OH)_3$ molecule is 0.0. HBs of $B(OH)_3$ with water molecules can only be formed in the planar direction of the $B(OH)_3$ molecule, which is consistent with the previous literature [45]. The schematic illustration of a $B(OH)_3$ molecule with its HB structure with the surrounding water molecules is shown in Fig. 6c. n_{HB} per $B(OH)_3$ molecule between $B(OH)_3$ and water molecules along the *z*-axis is shown in Fig. 6d. In the extremely confined slits with the width of 2.7 Å, n_{HB} per $B(OH)_3$ molecule is nearly unchanged when it passes through the hydroxylated and hydrogenated graphene slits. To maintain this HB interaction with water, the $B(OH)_3$ molecule will pass through the membrane with the molecular plane vertical to the membrane surface. Therefore, it can be concluded that slit-like pores can hardly reject $B(OH)_3$ molecules. As the $B(OH)_3$ and its HB structure with the surrounding water molecules are plate-like, it can also be concluded that the $B(OH)_3$ rejection is dependent on the major diameter of the non-circular pores (Fig. 6e). Therefore, the circular pore is the most suitable pore, which offers the narrowest major diameter to reject $B(OH)_3$ and the largest area for water permeation at the same time.

3.3. The effect of pore size on rejection

Using the circular TpPa-Rs pores, we then investigate the effect of pore size on the $B(OH)_3$ rejection. As discussed above, with comparable pore size of ~6 Å, the hydrophilic pores have >90% $B(OH)_3$ rejections, while the hydrophobic pores have <20% $B(OH)_3$ rejections (Fig. 3). In the hydrophilic pores with the terminal groups of COOH, NH_2, and OH, when the pore diameters are increased to ~8 Å, the $B(OH)_3$ rejections are decreased to 40.7%, 50.3%, and 37.2%, respectively (Fig. 7a). In the hydrophobic pores with the terminal groups of NO_2, SH, and CH_3, when the pore diameters are decreased to 2.9, 3.1, and 3.4 Å, respectively, the $B(OH)_3$ rejections are all increased to 100% (Fig. 7b). Therefore, to effectively reject $B(OH)_3$, the major diameters of the hydrophilic pores are ~6.4 Å, while those of the hydrophobic pores are ~3.1 Å. The rejection mechanism of the hydrophilic pores is discussed above. The

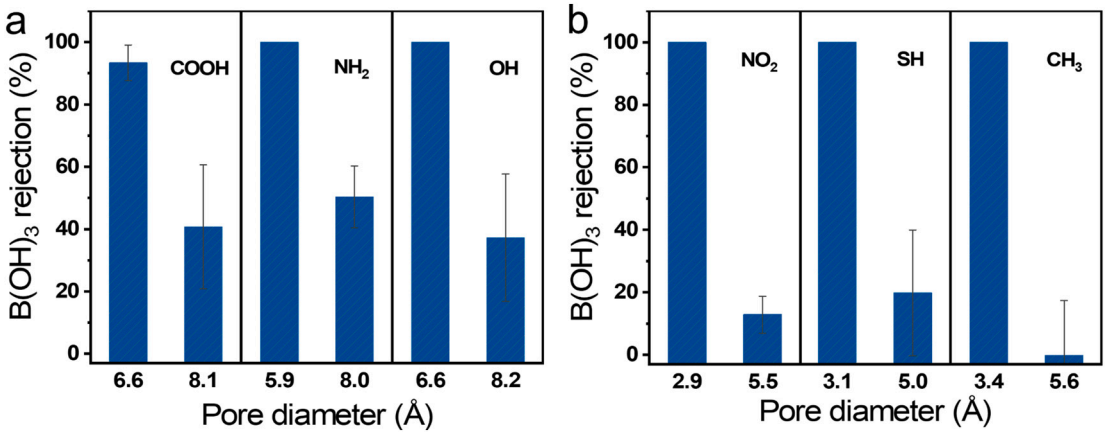

Fig. 7. The $B(OH)_3$ rejections of hydrophilic (a) and hydrophobic (b) pores of the TpPa-R membranes with various diameters.

rejection mechanism of hydrophobic pores can be ascribed to the size exclusion. This is because the diameters of the NO_2- and SH-functionalized pores are smaller than or equal to the Stokes diameters of $B(OH)_3$, 3.1 Å [11,41]. Besides, the CH_3-functionalized pore with a diameter of 3.4 Å shows a complete $B(OH)_3$ rejection because the very hydrophobic character of the pore wall provides smaller transporting paths (Fig. 5).

3.4. Water permeance

After investigating the effects of hydrophilicity, shape, and size of the pores on the $B(OH)_3$ rejection, we then analyze the water permeance. To reach >90% $B(OH)_3$ rejections, the circular pores functionalized by COOH, NH_2, OH, NO_2, SH, and CH_3 are 6.6, 5.9, 6.6, 2.9, 3.1, and 3.4 Å, respectively. The corresponding water permeances are shown in Fig. 8. The permeances of the hydrophilic pores are much higher than those of the hydrophobic pores. There are two reasons: i) the hydrophilic pores have larger pore diameters; ii) the hydrophilic pores provide higher water densities inside the pore (Fig. 5), resulting in more water paths [46,47]. The water permeance of the hydrophilic pores is 255–1778 L m^{-2} h^{-1} bar^{-1}, which is two to four orders of magnitude than the experimental polyamide membranes [14,16,17].

Since the reverse osmosis membranes need to effectively remove salts and $B(OH)_3$, as well as to achieve the goal of maximizing the water permeance simultaneously, the effects of pore hydrophilicity and pore shape should be discussed. With regards to the pore hydrophilicity, the hydrophilic pores are not beneficial to reject the salt ions because the PW atoms will compensate for their hydration shell, which reduces the energy barrier for ion passage [46]. However, the hydrophilic pores achieve higher water permeance due to the preferential water-pore interaction [46,47]. Balancing salt rejection and water permeance, the hydrophilic pores will achieve a better desalination performance [46,47]. Moreover, the hydrophilic pores are more effective at the $B(OH)_3$ rejection as discussed above. Therefore, considering salt rejection, water permeance as well as $B(OH)_3$ rejection, the hydrophilic pores are more likely to achieve a better comprehensive performance. Moreover, it should be noted that the interior resistance of hydrophilic channels to water should be considered when the effect of the pore length is considered [26].

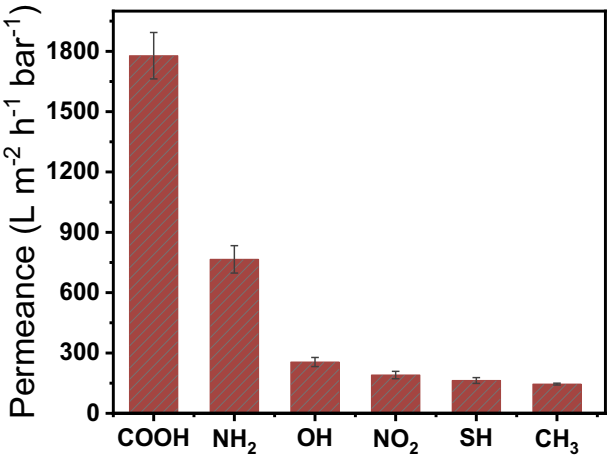

Fig. 8. Water permeance of TpPa-R membranes with different functional groups when the $B(OH)_3$ rejections are >90%.

With regards to the pore shape, the circular pore is the most suitable pore shape for the $B(OH)_3$ rejection as discussed above. Compared to the shape dependence, the salt rejection is primarily dependent on the energy barrier for the ion passage through a pore due to the dehydration of the strong and spherical hydration shell. Both the circular and slit pores can effectively reject salt ions [46,48]. Unlike rejecting $B(OH)_3$, the slit-like pore such as the elliptical pore may be more suitable for both the ion rejection and the water permeance. It was reported that increasing the area of the elliptical pore with a controlled minor diameter can enhance the water permeation without sacrificing the salt rejection [49].

4. Conclusions

The effects of hydrophilicity, shape, and size of sub-nanometer pores on the $B(OH)_3$ rejection are systematically investigated via NEMD simulations. Six types of functionalized COFs, namely TpPa-Rs, with different functional groups but comparable diameters of ~6.0 Å are used as models. It is found that the $B(OH)_3$ rejections of the hydrophilic pores with the functional groups of COOH, NH_2, and OH are >90%, while those of the hydrophobic pores with the functional groups of NO_2, SH, and CH_3 are <20%. The hydrophilic pores favor the $B(OH)_3$ rejection because they can preferentially adsorb water molecules due to the hydrogen bonding interaction, and the occupation of water molecules inside pores will block the $B(OH)_3$ molecules. To investigate the effect of the pore shape, the typical graphene slits are used as models in comparison with the circular TpPa-R pores. It is found that the $B(OH)_3$ rejections of the slit pores are ≤20% regardless of the hydrophilicity and slit width. The reason is that the $B(OH)_3$ and its HB structure with the surrounding water molecules are plate-like. Based on this unique structure, the circular pore is considered to be the most suitable for both high rejection of $B(OH)_3$ and high water permeance. Then, the effect of the size of the circular TpPa-R pores is investigated. To reach >90% rejection of $B(OH)_3$, the major diameters of hydrophilic pores with the functional groups of COOH, NH_2, and OH are 6.6, 5.9, and 6.6 Å, while those of the hydrophobic pores with functional groups of NO_2, SH, and

CH_3 are 2.9, 3.1, and 3.4 Å due to the separation mechanism of the size exclusion. This work suggests using circular and hydrophilic pores for efficient boron removal, which will be helpful to experimentally design and screen the next-generation membrane materials.

CRediT authorship contribution statement

Xin Zhang: Conceptualization, Investigation, Methodology, Software, Formal analysis, Validation, Writing - original draft. **Mingjie Wei**: Methodology, Writing - review & editing, Data curation, Visualization, Funding acquisition. **Yong Wang**: Writing - review & editing, Supervision, Funding acquisition.

Declaration of competing interest

The authors declare that they have no known competing financial interests or personal relationships that could have appeared to influence the work reported in this paper.

Acknowledgments

Financial support from the National Natural Science Foundation of China (21825803, 21921006) and the Jiangsu Natural Science Foundation (BK20190085). We thank the High Performance Computing Center of Nanjing Tech University for supporting the computational resources. We are also grateful to the Program of Excellent Innovation Teams of Jiangsu Higher Education Institutions and the Project of Priority Academic Program Development of Jiangsu Higher Education Institutions (PAPD).

Appendix A. Supplementary data

Atomic partial charges for the TpPa-Rs, illustration of steady-state water flows, the rejection of five-layered TpPa-R nanosheets, the HB autocorrelation functions, and comparison of the circular and triangular pores. Supplementary data to this article can be found online at doi:https://doi.org/10.1016/j.desal.2022.115755.

References

[1] M. Elimelech, W.A. Phillip, The future of seawater desalination: energy, technology, and the environment, Science 333 (2011) 712–717, https://doi.org/10.1126/science.1200488.
[2] E. Jones, M. Qadir, M.T.H. van Vliet, V. Smakhtin, S.-M. Kang, The state of desalination and brine production: a global outlook, Sci. Total Environ. 657 (2019) 1343–1356, https://doi.org/10.1016/j.scitotenv.2018.12.076.
[3] J.R. Werber, C.O. Osuji, M. Elimelech, Materials for next-generation desalination and water purification membranes, Nat. Rev. Mater. 1 (2016) 16018, https://doi.org/10.1038/natrevmats.2016.18.
[4] P. Glueckstern, M. Priel, Optimization of boron removal in old and new SWRO systems, Desalination 156 (2003) 219–228, https://doi.org/10.1016/S0011-9164(03)00344-8.
[5] F.S. Kot, Boron in the environment, Boron Sep. Process. (2015) 1–33, https://doi.org/10.1016/B978-0-444-63454-2.00001-0.
[6] Z. Ali, Y. Al Sunbul, F. Pacheco, W. Ogieglo, Y. Wang, G. Genduso, I. Pinnau, Defect-free highly selective polyamide thin-film composite membranes for desalination and boron removal, J. Membr. Sci. 578 (2019) 85–94, https://doi.org/10.1016/j.memsci.2019.02.032.
[7] A. Farhat, F. Ahmad, N. Hilal, H.A. Arafat, Boron removal in new generation reverse osmosis (RO) membranes using two-pass RO without pH adjustment, Desalination 310 (2013) 50–59, https://doi.org/10.1016/j.desal.2012.10.003.
[8] O. Nir, O. Lahav, Single SWRO pass boron removal at high pH: prospects and challenges, in: Boron Separation Processes, Elsevier, Haifa, Israel, 2015, pp. 297–323.
[9] Z. Guan, J. Lv, P. Bai, X. Guo, Boron removal from aqueous solutions by adsorption-a review, Desalination 383 (2016) 29–37, https://doi.org/10.1016/j.desal.2015.12.026.
[10] H.A. Abdulgader, V. Kochkodan, N. Hilal, Hybrid ion exchange - pressure driven membrane processes in water treatment: a review, Sep. Purif. Technol. 116 (2013) 253–264, https://doi.org/10.1016/j.seppur.2013.05.052.
[11] R. Bernstein, S. Belfer, V. Freger, Toward improved boron removal in RO by membrane modification: feasibility and challenges, Environ. Sci. Technol. 45 (2011) 3613–3620, https://doi.org/10.1021/es103991u.
[12] S. Shultz, V. Freger, In situ modification of membrane elements for improved boron rejection in RO desalination, Desalination 431 (2018) 66–72, https://doi.org/10.1016/j.desal.2017.08.021.
[13] S. Shultz, M. Bass, R. Semiat, V. Freger, Modification of polyamide membranes by hydrophobic molecular plugs for improved boron rejection, J. Membr. Sci. 546 (2018) 165–172, https://doi.org/10.1016/j.memsci.2017.10.003.
[14] S. Wang, Y. Zhou, C. Gao, Novel high boron removal polyamide reverse osmosis membranes, J. Membr. Sci. 554 (2018) 244–252, https://doi.org/10.1016/j.memsci.2018.03.014.
[15] P. Dydo, I. Nemś, M. Turek, Boron removal and its concentration by reverse osmosis in the presence of polyol compounds, Sep. Purif. Technol. 89 (2012) 171–180, https://doi.org/10.1016/j.seppur.2012.01.018.
[16] Y. Li, S. Wang, X. Song, Y. Zhou, H. Shen, X. Cao, P. Zhang, C. Gao, High boron removal polyamide reverse osmosis membranes by swelling induced embedding of a sulfonyl molecular plug, J. Membr. Sci. 597 (2020), 117716, https://doi.org/10.1016/j.memsci.2019.117716.
[17] L. Liu, X. Xie, S. Qi, R. Li, X. Zhang, X. Song, C. Gao, Thin film nanocomposite reverse osmosis membrane incorporated with UiO-66 nanoparticles for enhanced boron removal, J. Membr. Sci. 580 (2019) 101–109, https://doi.org/10.1016/j.memsci.2019.02.072.
[18] C. Chen, L. Jia, J. Li, L. Zhang, L. Liang, E. Chen, Z. Kong, X. Wang, W. Zhang, J.-W. Shen, Understanding the effect of hydroxyl/epoxy group on water desalination through lamellar graphene oxide membranes via molecular dynamics simulation, Desalination 491 (2020), 114560, https://doi.org/10.1016/j.desal.2020.114560.
[19] L. Liang, H. Zhou, J.-C. Li, Q. Chen, L. Zhu, H. Ren, Data-driven design of nanopore graphene for water desalination, J. Phys. Chem. C 125 (2021) 27685–27692, https://doi.org/10.1021/acs.jpcc.1c09470.
[20] H. Gao, J. Wang, X. Zhang, M. Hu, Q. Xu, Y. Xie, Y. Liu, R. Lu, Confined lamellar channels structured by multilayer graphene for high-efficiency desalination, Desalination 530 (2022), 115681, https://doi.org/10.1016/j.desal.2022.115681.
[21] Q. Liu, Y. Wu, X. Wang, G. Liu, Y. Zhu, Y. Tu, X. Lu, W. Jin, Molecular dynamics simulation of water-ethanol separation through monolayer graphene oxide membranes: significant role of O/C ratio and pore size, Sep. Purif. Technol. 224 (2019) 219–226, https://doi.org/10.1016/j.seppur.2019.05.030.
[22] X. Zhang, M. Wei, Z. Zhang, X. Shi, Y. Wang, Boron removal by water molecules inside covalent organic framework (COF) multilayers, Desalination 526 (2022), 115548, https://doi.org/10.1016/j.desal.2022.115548.
[23] S. Kandambeth, A. Mallick, B. Lukose, M.V. Mane, T. Heine, R. Banerjee, Construction of crystalline 2D covalent organic frameworks with remarkable chemical (acid/base) stability via a combined reversible and irreversible route, J. Am. Chem. Soc. 134 (2012) 19524–19527, https://doi.org/10.1021/ja308278w.
[24] M. Tong, Y. Lan, Q. Yang, C. Zhong, Exploring the structure-property relationships of covalent organic frameworks for noble gas separations, Chem. Eng. Sci. 168 (2017) 456–464, https://doi.org/10.1016/j.ces.2017.05.004.
[25] T.F. Willems, C.H. Rycroft, M. Kazi, J.C. Meza, M. Haranczyk, Algorithms and tools for high-throughput geometry-based analysis of crystalline porous materials, Microporous Mesoporous Mater. 149 (2012) 134–141, https://doi.org/10.1016/j.micromeso.2011.08.020.
[26] F. Xu, M. Wei, X. Zhang, Y. Wang, Effect of hydrophilicity on water transport through sub-nanometer pores, J. Membr. Sci. 611 (2020), 118297, https://doi.org/10.1016/j.memsci.2020.118297.
[27] E.A. Vogler, Structure and reactivity of water at biomaterial surfaces, Adv. Colloid Interf. Sci. 74 (1998) 69–117, https://doi.org/10.1016/S0001-8686(97)00040-7.
[28] Y. Tian, L. Jiang, Intrinsically robust hydrophobicity, Nat. Mater. 12 (2013) 291–292, https://doi.org/10.1038/nmat3610.
[29] F. Risplendi, F. Raffone, L.-C. Lin, J.C. Grossman, G. Cicero, Fundamental insights on hydration environment of boric acid and its role in separation from saline water, J. Phys. Chem. C 124 (2019) 1438–1445, https://doi.org/10.1021/acs.jpcc.9b10065.
[30] Z. Cao, V. Liu, A.Barati Farimani, Water desalination with two-dimensional metal–organic framework membranes, Nano Lett. 19 (2019) 8638–8643, https://doi.org/10.1021/acs.nanolett.9b03225.
[31] M. Heiranian, A.B. Farimani, N.R. Aluru, Water desalination with a single-layer MoS2 nanopore, Nat. Commun. 6 (2015) 8616, https://doi.org/10.1038/ncomms9616.
[32] S. Plimpton, Fast parallel algorithms for short-range molecular dynamics, J. Comput. Phys. 117 (1995) 1–19, https://doi.org/10.1006/jcph.1995.1039.
[33] H.W. Horn, W.C. Swope, J.W. Pitera, J.D. Madura, T.J. Dick, G.L. Hura, T. Head-Gordon, Development of an improved four-site water model for biomolecular simulations: TIP4P-ew, J. Chem. Phys. 120 (2004) 9665–9678, https://doi.org/10.1063/1.1683075.
[34] S.L. Mayo, B.D. Olafson, W.A. Goddard, DREIDING: a generic force field for molecular simulations, J. Phys. Chem. 94 (1990) 8897–8909, https://doi.org/10.1021/j100389a010.
[35] M. Tong, Q. Yang, Y. Xiao, C. Zhong, Revealing the structure-property relationship of covalent organic frameworks for CO2 capture from postcombustion gas: a multiscale computational study, Phys. Chem. Chem. Phys. 16 (2014) 15189–15198, https://doi.org/10.1039/C4CP02047B.
[36] L.C. Lin, J. Choi, J.C. Grossman, Two-dimensional covalent triazine framework as an ultrathin-film nanoporous membrane for desalination, Chem. Commun. 51 (2015) 14921–14924, https://doi.org/10.1039/C5CC05969K.
[37] W. Zhou, M. Wei, X. Zhang, F. Xu, Y. Wang, Fast desalination by multilayered covalent organic framework (COF) nanosheets, ACS Appl. Mater. Interfaces 11 (2019) 16847–16854, https://doi.org/10.1021/acsami.9b01883.
[38] T. Lu, F. Chen, Multiwfn: a multifunctional wavefunction analyzer, J. Comput. Chem. 33 (2012) 580–592, https://doi.org/10.1002/jcc.22885.

[39] W.L. Jorgensen, D.S. Maxwell, J. Tirado-Rives, Development and testing of the OPLS all-atom force field on conformational energetics and properties of organic liquids, J. Am. Chem. Soc. 118 (1996) 11225–11236, https://doi.org/10.1021/ja9621760.
[40] T. Darden, D. York, L. Pedersen, Particle mesh ewald: an N· log (N) method for ewald sums in large systems, J. Chem. Phys. 98 (1993) 10089–10092, https://doi.org/10.1063/1.464397.
[41] J.K. Park, K.J. Lee, Diffusion coefficients for aqueous boric acid, J. Chem. Eng. Data 39 (1994) 891–894, https://doi.org/10.1021/je00016a057.
[42] J. Muscatello, F. Jaeger, O.K. Matar, E.A. Müller, Optimizing water transport through graphene-based membranes: insights from nonequilibrium molecular dynamics, ACS Appl. Mater. Interfaces 8 (2016) 12330–12336, https://doi.org/10.1021/acsami.5b12112.
[43] R.H. Tunuguntla, R.Y. Henley, Y.-C. Yao, T.A. Pham, M. Wanunu, A. Noy, Enhanced water permeability and tunable ion selectivity in subnanometer carbon nanotube porins, Science 357 (2017) 792–796, https://doi.org/10.1126/science.aan2438.
[44] X. Zhang, W. Zhou, F. Xu, M. Wei, Y. Wang, Resistance of water transport in carbon nanotube membranes, Nanoscale 10 (2018) 13242–13249, https://doi.org/10.1039/C8NR03116A.
[45] Y. Zhou, T. Yamaguchi, W. Zhang, K. Ikeda, K. Yoshida, F. Zhu, H. Liu, The structural elucidation of aqueous H3BO3 solutions by DFT and neutron scattering studies, Phys. Chem. Chem. Phys. 22 (2020) 17160–17170, https://doi.org/10.1039/D0CP02306J.
[46] D. Cohentanugi, J.C. Grossman, Water desalination across nanoporous graphene, Nano Lett. 12 (2012) 3602, https://doi.org/10.1021/nl3012853.
[47] K. Zhang, Z. He, K.M. Gupta, J. Jiang, Computational design of 2D functional covalent-organic framework membranes for water desalination, Environ. Sci.: Water Res. Technol. 3 (2017) 735–743, https://doi.org/10.1039/C7EW00074J.
[48] B. Chen, H. Jiang, X. Liu, X. Hu, Molecular insight into water desalination across multilayer graphene oxide membranes, ACS Appl. Mater. Interfaces 9 (2017) 22826–22836, https://doi.org/10.1021/acsami.7b05307.
[49] Q. Lyu, S. Sun, C. Li, S. Hu, L.C. Lin, Rational design of two-dimensional hydrocarbon polymer as ultrathin-film nanoporous membranes for water desalination, ACS Appl. Mater. Interfaces 10 (2018) 18778–18786, https://doi.org/10.1021/acsami.8b04630.